The Journal of Chemical Physics

Infrared frequency comb spectroscopy of CH_2I_2: Influence of hot bands and pressure broadening on the ν_1 and ν_6 fundamental transitions

Cite as: J. Chem. Phys. **156**, 114301 (2022); https://doi.org/10.1063/5.0081836
Submitted: 10 December 2021 • Accepted: 21 February 2022 • Accepted Manuscript Online: 22 February 2022 • Published Online: 15 March 2022

Frances C. Roberts and Julia H. Lehman

The Journal of Chemical Physics ARTICLE scitation.org/journal/jcp

Infrared frequency comb spectroscopy of CH_2I_2: Influence of hot bands and pressure broadening on the ν_1 and ν_6 fundamental transitions

Cite as: J. Chem. Phys. 156, 114301 (2022); doi: 10.1063/5.0081836
Submitted: 10 December 2021 • Accepted: 21 February 2022 •
Published Online: 15 March 2022

Frances C. Roberts and Julia H. Lehman[a)]

AFFILIATIONS

School of Chemistry, University of Leeds, Leeds, United Kingdom

Note: This paper is part of the 2022 JCP Emerging Investigators Special Collection.
[a)]**Author to whom correspondence should be addressed:** j.lehman@leeds.ac.uk

ABSTRACT

Direct frequency comb spectroscopy was utilized to measure the vibrational absorption spectrum of diiodomethane, CH_2I_2, from 2960 to 3125 cm^{-1}. The data were obtained using a CH_2I_2 concentration of $(6.8 \pm 1.3) \times 10^{15}$ molecule cm^{-3} and a total pressure of 10–300 mbar with either nitrogen or argon as the bath gas. The rovibrational spectra of two fundamental transitions, ν_6 and ν_1, were recorded and analyzed. We suggest that a significant contribution to the observed congested spectra is due to the population in excited vibrational states of the low energy ν_4 I–C–I bend, resulting in transitions $6^1_0 4^n_n$ and $1^1_0 4^n_n$, where the integer n is the initial vibrational level v = 1–5. PGOPHER was used to fit the experimental spectrum, allowing for rotational constants and other spectral information to be reported. In addition, it was found that the peak widths for the observed transitions were limited by pressure broadening, resulting in a pressure broadening parameter of (0.143 ± 0.006) cm^{-1} atm^{-1} by N_2 and (0.116 ± 0.006) cm^{-1} atm^{-1} by Ar. Further implications for other dihaloalkane infrared spectra are discussed.

I. INTRODUCTION

Diiodomethane, CH_2I_2, is a significant contributor to the global iodine budget, especially in coastal locations and in the marine boundary layer.[1–6] This dihalogen organic compound has a relatively short atmospheric lifetime (2–10 min)[7] due to rapid photolysis to form CH_2I, I, and CH_2. These products, in particular, the iodine radical, then influence important atmospheric processes such as ozone depletion, aerosol formation, and the NO_x and HO_x cycles via reactions with the IO radical, which is readily formed through reactions of the iodine radical with ozone.[5,6,8–10] Aside from its atmospheric importance, CH_2I_2 is now commonly used in laboratory experiments[11] as an effective precursor to generate the smallest Criegee intermediate, CH_2OO, through the reaction of CH_2I with O_2.

Despite its continued use in laboratory environments and importance in the marine boundary layer, fundamental gas phase spectroscopic studies of CH_2I_2, specifically in the infrared, are somewhat lacking. Understandably, a more significant effort has been made toward understanding its electronic spectroscopy (for example, Refs. 7, 12–14 and references thereof), with comparably less information available on its rotational[15,16] and vibrational spectroscopies.[17–21] The most recent gas phase infrared study reported spectra at two temperatures (298.15 and 323.15 K)[17,19] and measured quantitative absorption cross sections from 530–7100 cm^{-1}, which is included in the HITRAN database.[22] However, the published work was conducted at atmospheric pressure, which obscured a spectroscopic detail due to pressure broadening of the rovibrational transitions, limiting the information gathered to absorption cross section, band type, and band origin with an uncertainty of ±0.1 cm^{-1}. Although this previous work did not report rotational constants for the observed transitions, a further study[23] on the IR spectrum from 2250–3400 cm^{-1} had a spectral resolution of 0.002 cm^{-1} and was able to extract rotational constants for the ν_6 and ν_1 bands, but is unpublished. Some vibrational information for CH_2I_2 can be found within references that focus on the influence of vibrational relaxation and redistribution within electronic energy levels,[12,24] but these studies do not report other properties, such as rotational constants of specific vibrational modes. Theoretical studies are also fairly limited on CH_2I_2 vibrational spectroscopy. However, one particular study[25] used the internal coordinate model to calculate anharmonic vibrational

frequencies of fundamental and overtone bands, which showed good agreement between theory and low resolution observations. Solution phase[26–30] and solid state[31–33] infrared spectra have also been reported, but were either low resolution or were focused on vibrational relaxation and energy transfer.

Other dihalomethanes with the structure CH_2X_2 (where X = F, Cl, or Br) have been the subject of numerous publications focused on fundamental infrared spectroscopy plus other areas of electronic and rotational spectroscopy.[21,31,34–54] The C–H stretching region of the infrared spectrum of difluoromethane, CH_2F_2, for example, is of great interest in understanding Coriolis coupling and Fermi resonances, where the ν_1, ν_6, $2\nu_2$, $2\nu_8$, and $\nu_2 + \nu_8$ transitions are all within 200 cm^{-1} of each other (see Ref. 36 and references therein). However, when moving to CH_2Cl_2, this molecule was noted as "an almost vibrationally unperturbed molecule" (for example, see Refs. 40 and 54 and references thereof). CH_2Br_2 was also shown to have no perturbations within the C–H stretching region.[43] However, both CH_2Cl_2 and CH_2Br_2 have other complicating factors when analyzing these spectra since both the halogens have two stable isotopes, leading to three different isotopologs present within normal isotopic abundance samples. Iodine, however, is monoisotopic, so the rovibrational spectrum of CH_2I_2 should not suffer from the same level of spectral congestion and complicated levels of analysis.

In this work, we utilize a frequency comb laser combined with a spatially dispersive spectrometer to measure a high-resolution CH_2I_2 infrared spectrum over the range of 2950–3130 cm^{-1}. Frequency comb spectroscopy is an emerging technique in the chemical sciences. There are several benefits of frequency comb spectroscopy over traditional Fourier transform infrared (FTIR) spectroscopy or using single frequency lasers scanned over a broad spectral range. For example, frequency comb spectrometers generally achieve a better signal-to-noise ratio during the collection of a broadband, high-resolution spectrum than traditional techniques in the same amount of averaging time. There are also potential advantages in achievable spectral resolution, depending on the spectrometer, in comparison to traditional techniques. Please see review articles (Refs. 55–57) and book chapter (Ref. 58) for further information. Here, we use our recently built frequency comb spectrometer to extract rotational constants, band origins, and other spectroscopic parameters. In addition, we explore the impacts of pressure broadening on the observed spectrum. Information gathered from the analysis of the CH_2I_2 spectrum is then compared to other dihalomethane spectra.

II. EXPERIMENTAL METHODS

The experimental apparatus has been discussed previously,[59] and therefore, only a brief description follows. The laser (Menlo Systems) is a mode-locked, femtosecond frequency comb laser operating with a 250 MHz repetition rate.[60] Difference frequency generation is used to produce the mid-infrared frequency comb laser, spanning 2700 to 3300 cm^{-1} (3000–3500 nm). The individual frequencies (f_n) of the comb spanning the broadband output of the laser are integer (n) multiples (f_{rep}) such that $f_n = n \cdot f_{rep}$. Each comb tooth is separated from the next by the repetition rate, which is tunable around 250 MHz (or 0.0083 cm^{-1}).

The laser beam is directed through a Herriott multipass gas cell. Calibration of the path length through a gaseous sample is achieved by multiple measurements of various known CH_4 concentrations, resulting in a path length measurement of 570 ± 60 cm. After exiting the Herriott cell, the laser beam is then fiber coupled to the imaging detection setup, where the beam is spatially dispersed using the combination of a VIPA (virtually imaged phase array, Light Machinery)[61] and a diffraction grating as a cross-dispersive element. The resulting 2D array of frequency comb modes (comb "teeth") is imaged onto an InSb infrared camera (Infratec). Calibration of each frequency comb mode number (integer n, as above) imaged on the camera is achieved using the infrared spectrum of CH_4. See our previous study[59] for an in-depth discussion of the frequency axis calibration. As a submultiple of the frequency comb repetition rate is locked to a rubidium clock (10 MHz, Stanford Research Systems), this sets the accuracy for the frequency of each comb mode.[59,62]

In order to record the mid-IR spectrum shown in this work, spanning 2950 up to 3130 cm^{-1}, six different grating positions (grating angle with respect to the camera) were used, which will be referred to as separate windows. For each window, three repetition rates of the frequency comb laser were used: 249.9999, 250.0000, and 250.0001 MHz. This allows for a data point separation of 0.0028 cm^{-1} once the three datasets are interleaved. For each repetition rate in each window, 10 000 images (50 μs exposure time for one image, 125 Hz camera imaging rate) were averaged together for both signal (CH_2I_2 present with buffer gas) and background (N_2 only) datasets. The same datasets were taken for the frequency calibration measurements with CH_4.

A pure flow of N_2 is used as the background spectrum to ensure all impurities are removed from the gas cell. Either argon or N_2 is used as the bath gas for the CH_2I_2 sample in the two experiments reported here, which consist of detailed spectral analysis and pressure broadening experiments. In both the experiments, flowing samples were used, with the pressure in the cell controlled by mass flow controllers and an in-line control valve prior to the vacuum pump. Using a gas flow over a liquid sample of CH_2I_2 (Sigma-Aldrich, 99% pure), the concentration of CH_2I_2 was determined via its known vapor pressure (1.6 mbar at 298 K).[63] As the vapor pressure of CH_2I_2 is low at room temperature, the sample was heated within the Teflon (PTFE)-lined sample container to ~313 K, yielding a vapor pressure of 6.15 mbar. As Teflon has fairly poor thermal conductivity, leading to uncertainties in the vapor pressure of CH_2I_2, the CH_2I_2 concentration was further verified by comparison with the previously reported absorption cross section combined with our measured absorption path length (discussed in Sec. IV B). For the detailed spectral analysis experiment, Ar was used as the bath gas. Each spectrum was recorded at room temperature, with a total pressure of 11.3 ± 0.1 mbar in the cell and a CH_2I_2 concentration of $(6.8 \pm 1.3) \times 10^{15}$ molecule cm^{-3} or 0.28 ± 0.05 mbar. In the second experiment, focused on the effects of pressure broadening, both N_2 and Ar were used as a bath gas. Here, gas cell pressures ranged from 20 to 1000 mbar, while the CH_2I_2 concentration was kept approximately constant at $(2.7 \pm 0.5) \times 10^{14}$ molecule cm^{-3}. The errors reported for the two concentrations of CH_2I_2 are based on the error of the mass flow controller, the vapor pressure, and do not include the possible systematic errors discussed in Sec. IV B.

As discussed previously,[59] the data acquired for each window are recorded in the form of a 560 × 640 pixel thermal image. In order to transform the image into a spectrum, a *MATLAB* code is used to analyze the integrated intensity (I for the signal and I_0 for

the background) of each frequency comb mode, order the modes in ascending frequency wavenumber, and then use the Beer–Lambert law to determine the absorption spectrum [absorption = $\ln(I/I_0)$] for that particular window and frequency comb repetition rate. This process is then repeated for all 18 datasets. Further spectral data processing is needed in the form of a fast Fourier transform filter for some external background noise, which is applied to all windows and repetition rates. The background noise near 840 MHz is due to an unknown source and is visible on datasets with and without the sample present. When this noise is filtered, the baseline noise reduces from 4.92×10^{-4} to 2.35×10^{-4}. The filtered data for each window are interleaved for the three frequency comb repetition rates, which gives six spectra with a data point spacing of 0.0028 cm^{-1}. Finally, these six spectra are combined to form one full spectrum, where overlapping sections having an average of 7 cm^{-1} of overlapping data points between adjacent windows are averaged together to give the final spectrum.

To analyze the acquired CH_2I_2 spectrum, the program PGOPHER[64] was implemented concentrating on two different spectral fitting methods: the line-position fitting procedure and contour fitting. The line-position fitting procedure within PGOPHER is recommended for determining rotational constants, especially with high-resolution spectra. This requires a rotational–vibrational line list to be generated for the corresponding vibrational transition, whereby each simulated peak is assigned to a corresponding experimental peak. Each rotational constant and the origin are then individually fitted in accordance with the generated line list. For each upper vibrational state described below, seven parameters have been fitted via line-position fitting, using a Watson S reduction Hamiltonian: origin, A, $\overline{B}$, δ [where $\overline{B} = {}^1/_2(B + C)$ and $\delta = (B - C)$], D_J, D_{JK}, and D_k. Furthermore, for each lower vibrational state described below, all the rotational constants have been taken from available rotational spectra (A, $\overline{B}$, δ, D_J, D_{JK}, D_K, δK, δJ, H_J, H_{JK}, H_{KJ}, and H_K).[15,16] The last six of these rotational constants for each lower vibrational state have been included for the upper vibrational state, but not fitted, as the lack of well-resolved higher K_a transitions makes it difficult to fit the constants to a reasonable level of certainty. For each of the fitted rotational constants, the error is the standard deviation based on the quality of the fit given by PGOPHER.[64] After the successful determination of spectroscopic parameters via line-position fitting, contour fits within PGOPHER work by fitting the overall shape of the simulated spectrum to the experimental spectrum. This method is not recommended for robust fitting of the rotational constants but was used to fit overall pressure broadening parameters by allowing the peak width parameter to be fitted to the data from the second experiment. Further information on how both of these procedures work can be found within PGOPHER documentation.[64]

III. RESULTS

Figure 1 shows the recorded rovibrational spectrum for CH_2I_2 from 2960 to 3125 cm^{-1}. This experimental spectrum is a culmination of all 36 individual spectra, as discussed in the Sec. II: six grating positions ("windows") each taken at three different frequency comb repetition rates, in duplicate for a signal image (with CH_2I_2 present) and a background image (N_2 only). The y-axis shows an absorption cross section, as determined for a specified temperature and total pressure by $\sigma_\nu = \ln(\tau_\nu)/\rho L$, where σ_ν is the absorption cross section (cm^2 $molecule^{-1}$) at wavenumber ν, τ is the spectral transmittance at wavenumber ν, and ρ is the density (molecule cm^{-3}) along an optical path of length, L (cm), as used by HITRAN.[17,19,22]

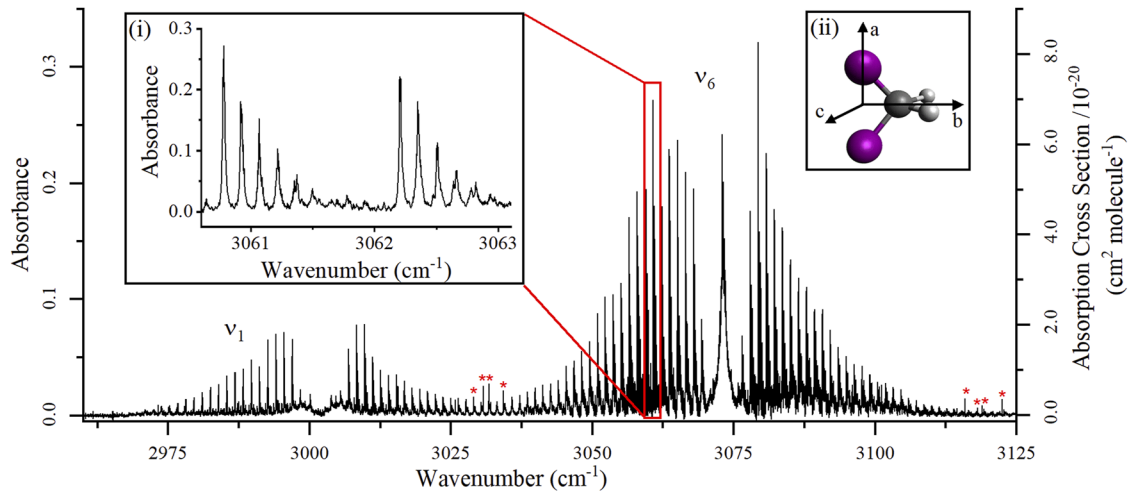

FIG. 1. Full experimental CH_2I_2 vibrational spectrum from 2960 to 3125 cm^{-1} under the following conditions: 298 K, path length of 570 ± 60 cm, and CH_2I_2 partial pressure of 0.28 ± 0.05 mbar, with a total pressure of 11.3 ± 0.1 mbar. Red asterisks indicate impurities observed with or without the CH_2I_2 sample present. The left y-axis shows the absorbance measured in this work, and the right y-axis shows the absorbance cross section (cm^2 $molecule^{-1}$) based on the corrected experimental concentration and path length. (i) Expanded region of the ν_6 C–H asymmetric stretch from 3060.5 to 3063.5 cm^{-1}. This region shows two transitions: $^PQ_9(J)$ and $^PQ_8(J)$. (ii) Molecular structure of CH_2I_2 (iodine = purple, carbon = gray, and hydrogen = white). The axes show the labels used for this analysis: the ν_6 asymmetric stretch causes a transition dipole moment along the c axis, and the ν_1 symmetric stretch causes a transition dipole moment along the b axis.

Inset (i) of Fig. 1 shows an expansion of the spectrum indicated by the red box, and inset (ii) shows CH_2I_2 superimposed on the rotational axis system used during the analysis presented below. Note that CH_2I_2 is a near prolate asymmetric top molecule with C_{2v} symmetry, with a value of $\kappa = -0.9986$, where $\kappa = (2B - A - C)/(A - C)$, based on the ground vibrational state rotational constants measured by microwave spectroscopy.[16] The majority of the analysis, such as fitting procedures and determining rotational constants, was performed in the program PGOPHER as described above.

Within this wavenumber region of the infrared, there are two vibrational bands immediately evident: the fundamental ν_1 transition visible from 2967 to 3032 cm^{-1} and the fundamental ν_6 transition from 3032 to 3115 cm^{-1}. These normal modes can nominally be described as symmetric (ν_1) and antisymmetric (ν_6) C–H stretches of the CH_2 moiety. The ν_1 band has well-defined $^{P/R}Q_{Ka}(J)$ branches, with no central Q branch, consistent with the fact that ν_1 is a b-type transition with a_1 symmetry as previously reported.[17] On the other hand, the ν_6 band has a strong, central Q branch, and then, $^{P/R}Q_{Ka}(J)$ branches, which is consistent with ν_6 being a c-type transition with b_1 symmetry, again as previously reported.[17] Summing across each vibrational band to obtain integrated absorption coefficients, values of 3.21×10^{-19} cm^2 $molecule^{-1}$ for ν_6 (from 3045.003 to 3099.999 cm^{-1}) and 7.32×10^{-20} cm^2 $molecule^{-1}$ for ν_1 (from 2970.003 to 3028.001 cm^{-1}) are obtained. It should be noted that these slightly reduced regions were chosen to minimize the inclusion of water impurity peaks and overlapping regions of the two vibrational bands, so they should be considered a lower limit. This gives a band strength ratio of 1:0.23 for ν_6:ν_1, which agrees well with the reference data (supplementary material, Sec. C). Within each vibrational band, there are a series of peaks. Each peak consists of many transitions that, due to line broadening, appear as one peak with a full-width-at-half-maximum (FWHM) of ~0.02 cm^{-1}. The major source of the line broadening is likely to be pressure broadening, discussed further below (see Sec. III C). The abundance of peaks seen as repeating stacks were initially unexpected (Fig. 2, inset), hereafter referred to as progressions. In the previous study,[17] the atmospheric pressure used meant these progressions presented as one single broad peak (approximate FWHM of 0.3 cm^{-1}), albeit with an asymmetrical line shape. Evidence of this can be seen in Fig. C1 in the supplementary material, where the previously reported spectrum (HITRAN data) is superimposed on the experimental data. Similar progressions are present in the high-resolution spectrum of CH_2Br_2.[42] The different peaks within the progressions were attributed to the three isotopomers of the molecule. However, this argument fails for CH_2I_2 due to the monoisotopic nature of iodine. Therefore, a different argument is needed to explain the peak progressions observed in the experimental spectrum presented here.

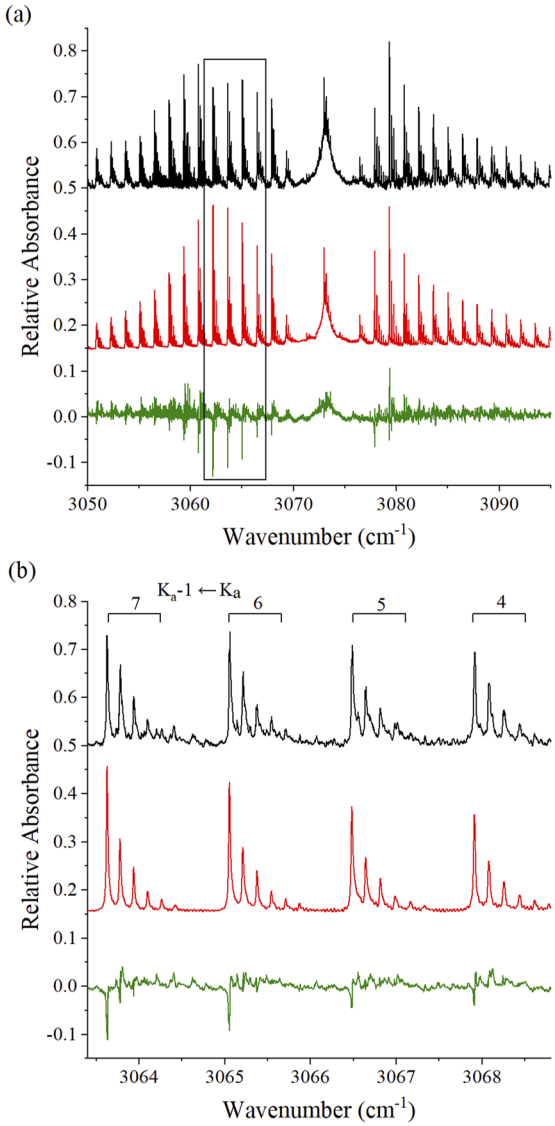

FIG. 2. (a) Comparison of the experimental spectrum (black) and the overall simulation (red), as determined in PGOPHER, for the ν_6 band from 3050 to 3095 cm^{-1}. The overall simulation is compiled of the different simulated transitions for the fundamental 6^1_0 band and the $6^1_0\ 4^n_n$ hot bands, where $n \leq 5$. The y-axis shows relative absorbance of the experimental and simulation spectra, where the simulation has been scaled up to match the experimental. The green line is the residual plot of experimental minus the overall simulation. (b) Zoomed-in portion of the three spectra, from 3062.4 to 3068.7 cm^{-1}, showing four different K_a transitions in the ^PQ branch.

A. Fitting results of the ν_6 band

For the ν_6 vibrational band, the discernible peaks span 3032 up to 3115 cm^{-1}, with the band origin at 3072.912 cm^{-1}. Assuming a conservative minimum detectable absorption of 3σ above the baseline noise ($\sigma = 2.4 \times 10^{-4}$), ~210 peaks in this band are detectable. These peaks involve a strong central Q branch and $^{P/R}Q_{Ka}(J)$ branches that are spaced by ~$2(A - \overline{B})$. For c-type transitions, using the inertial axes as labeled in Fig. 1[inset (ii)], the rotational selection rules are: $\Delta J = 0, \pm1$, $\Delta K_a = \pm1$, and $\Delta K_c = 0, \pm2$.

To assign the fundamental transitions of the ν_6 band, we use a fitting procedure within PGOPHER[64] as described in the Sec. II. This procedure involves manually assigning the experimental peaks to the corresponding simulation peaks and allowing the program to perform a line fitting function while

TABLE I. Experimentally determined rotational constants for the fundamental ν_6 and ν_1 vibrational bands. The standard deviation error is given in brackets for each constant. All values are given in cm^{-1}.

	Ground state (v = 0)[a]	ν_6 (v = 1)	ν_1 (v = 1)
Origin	⋯	3072.906(3)	3 001.940 7(4)
A	0.734 994 042	0.735 004(2)	0.733 603(3)
$\overline{B}$	0.020 453 481	0.020 454 9(4)	0.0204 527(1)
δ	0.000 493 192	0.000 493(6)	0.000 498(3)
$D_K \times 10^{-5}$	1.186 01	1.201(2)	1.180(1)
$D_{JK} \times 10^{-7}$	−2.149 26	−2.13(2)	−2.103(7)
$D_J \times 10^{-9}$	2.291 97	2.23(6)	2.26(2)

[a]Constants from Ref. 15.

varying the required parameters, such as rotational and centrifugal distortion constants. The final constants are documented in Table I alongside the ground state constants used within the program, which were taken directly from the microwave data in Ref. 15. The overall simulated spectrum produced from this fitting algorithm can be seen in Fig. 2. Due to pressure broadening, each peak is a combination of many (J, K_c) transitions that share a common K_a transition.

We have observed that for each repeating progression in the ν_6 band, there are up to six detectable peaks. The highest intensity peak always belongs to the 6^1_0 vibrational transition, but the progressions are being caused by additional vibrational transitions. Taking into consideration all nine fundamental normal mode vibrations of CH_2I_2 (see Table II), the lowest energy vibrational mode is the ν_4 ICI bending mode (121 cm^{-1} for Raman and liquid IR studies[17] and 127 cm^{-1} for the crystalline phase[32]). This transition wavenumber is less than the available thermal energy at room temperature ($k_BT \approx 200\ cm^{-1}$), which means it is reasonable to assume that ν_4 has population in excited vibrational states during the experiment. Further discussion of the expected Boltzmann population distribution, which is automatically calculated in the PGOPHER simulation for a given temperature, is in Sec. IV E.

The population in these ν_4 (v > 0) states can then be excited with a transition frequency similar to that of the fundamental ν_6 transition. In other words, the transition would be denoted $6^1_0 4^1_1$ for population initially in ν_4 (v = 1) and will be referred to as hot bands. These are not technically combination bands since only one vibrational quantum number changes in the transition, although cross-anharmonicity terms would still be present and impact the observed transition frequency. Including these transitions in an overall simulation, using ν_4 (v ≤ 4) rotational constants from Ref. 15, gives a very good match to the experimental spectrum, as seen in Fig. 2. The ν_4 (v = 5) rotational constants were extrapolated from the ν_4 (v ≤ 4) rotational constants reported in Ref. 15. However, as there has been no gas phase studies involving the ν_4 vibration, the transition energy for 4^1_0 was approximated to 121 cm^{-1} (the same for the liquid IR studies), and the subsequent transitions are just integer multiples of 121 cm^{-1}, for example, 242 cm^{-1} for the 4^2_0 transition. This approximation does not significantly impact the simulated spectrum since the $6^1_0 4^n_n$ origin is fit during the procedure, although the intensity of the $6^1_0 4^n_n$ transitions will be impacted since these are dependent on the PGOPHER calculated

TABLE II. Vibrational normal mode assignments for previous work compared to this work. All vibrational wavenumbers (cm^{-1}) are based on the gas phase IR assignments unless otherwise stated.

	Symmetry	Experiment	wB97X/Def2QZVPP[a]
ν_4	a_1	122[b]	122.802
		127[c]	
		121[d]	
ν_3	a_1	493.01[e]	515.672
		486[f]	
ν_9	b_2	584.21[e]	634.548
		572[f]	
		585[g]	
ν_7	b_1	718.08[e]	808.653
		717[f]	
		717[g]	
ν_5	a_2	1041.99[e]	1077.289
		1035[f]	
ν_8	b_2	1113.87[e]	1160.892
		1108[f]	
		1113.5[g]	
ν_2	a_1	1373.61[e]	1453.997
		1351[f]	
		1230[g]	
ν_1	a_1	3001.9407(4)[a]	3133.216
		3002.00[e]	
		2967[f]	
ν_6	b_1	3072.906(3)[a]	3196.503
		3073.01[e]	
		3049[f]	
		3074[g]	

[a]This work.
[b]Liquid IR, Ref. 17.
[c]Liquid IR, Ref. 32.
[d]Liquid IR, Ref. 20.
[e]Reference 17.
[f]Reference 21, ν_3 and ν_2 have been relabeled to remain consistent with other literature.
[g]Reference 18.

Boltzmann population distribution, based on a rotational temperature of 300 K, and the calculated line strengths, *S*. The supplementary material (Sec. B) shows the breakdown of the individual simulated spectra for each $6^1_0 4^n_n$ transition, where n ≤ 5. It is unfortunately not possible to determine the vibrational band origins for ν_4 since we do not change the vibrational quantum number for ν_4 in the observed $6^1_0 4^n_n$ transitions. A further discussion of this is found in the supplementary material (Sec. E).

The residual plot shown in Fig. 2 (green line) indicated that there is good agreement between the overall fit of the simulated spectrum to the experimental spectrum, but currently shows a mismatch in the observed relative intensities, especially in the $^PQ_{Ka}(J)$ branch. The $^PQ_{Ka}(J)$ branch over the 3060 to 3070 cm^{-1} range was recorded several times over several weeks, but did not show significant differences in the peak relative intensities. It is unclear what the reasoning could be for the difference in peak intensity patterns here and why the simulation does not capture this intensity pattern. It is noted that

TABLE III. Experimentally determined rotational constants for the hot bands of ν_6 (v = 1) + ν_4 (v ≤ 5) and ν_1 (v = 1) + ν_4 (v ≤ 4). The standard deviation error is given in brackets for each constant. All values are given in cm^{-1}. Rotational constants for the ν_4 (v ≤ 5) bands are taken from Ref. 15.

	ν_6 (v = 1) + ν_4 (v = 1)	ν_6 (v = 1) + ν_4 (v = 2)	ν_6 (v = 1) + ν_4 (v = 3)	ν_6 (v = 1) + ν_4 (v = 4)	ν_6 (v = 1) + ν_4 (v = 5)
Origin	3194.093 6(9)	3315.291(1)	3436.489(1)	3557.691(1)	3678.876(1)
A	0.737 785(7)	0.740 639(8)	0.743 45(1)	0.746 34(1)	0.749 40(2)
$\overline{B}$	0.020 448 5(1)	0.020 440 4(1)	0.020 433 3(1)	0.020 425 1(1)	0.020 416 8(1)
δ	0.000 495 1(5)	0.000 495 0(7)	0.000 495 0(9)	0.000 495(2)	0.000 494 0(7)
$D_K \times 10^{-5}$	1.216(2)	1.219(2)	1.222(2)	1.226(4)	1.224(9)
$D_{JK} \times 10^{-7}$	−2.158(9)	−2.19(1)	−2.225(9)	−2.29(1)	−2.33(2)
$D_J \times 10^{-9}$	2.241(2)	2.23(1)	2.18(2)	2.17(2)	2.13(2)
	ν_1 (v = 1) + ν_4 (v = 1)	ν_1 (v = 1) + ν_4 (v = 2)	ν_1 (v = 1) + ν_4 (v = 3)	ν_1 (v = 1) + ν_4 (v = 4)	ν_1 (v = 1) + ν_4 (v = 5)
Origin	3123.0288(8)	3244.1060(7)	3365.185(2)	3486.246(1)	⋯
A	0.736 356(8)	0.739 179(6)	0.742 023(2)	0.744 904(1)	⋯
$\overline{B}$	0.020 445 8(1)	0.020 438 34(9)	0.020 430 8(3)	0.020 424 1(1)	⋯
δ	0.000 049 0(2)	0.000 50(1)	0.000 51(1)	0.000 52(1)	⋯
$D_K \times 10^{-5}$	1.201(3)	1.2251(2)	1.2663(8)	1.299(6)	⋯
$D_{JK} \times 10^{-7}$	−2.22(1)	−2.19(1)	−2.18(3)	−2.17(2)	⋯
$D_J \times 10^{-9}$	2.28(2)	2.25(2)	2.23(4)	2.21(2)	⋯

for both 6^1_0 and 1^1_0 (discussed below), the residual plots show larger disagreement with the $^PQ_{Ka}(J)$ branch than the $^RQ_{Ka}(J)$ branch. The shape of the residuals indicates that it is not a result of peak position or width mismatch, but instead primarily peak intensity. This points to a possible perturbation that is not recovered in the PGOPHER simulation. The experimentally determined rotational constants for the $6^1_0 4^n_n$ transitions are included in Table III.

B. Fitting results of the ν_1 band

For the ν_1 vibrational band, the discernible peaks span 2967 to 3032 cm^{-1}, with the band origin at 3001.912 cm^{-1}. Again, assuming a conservative minimum detectable absorption of 3σ above the baseline noise ($\sigma = 2.4 \times 10^{-4}$), ~100 peaks in this band are detectable. These transitions are evenly spaced across $^{P/R}Q_{Ka}(J)$ branches that are spaced by ~2(A − $\overline{B}$). For b-type transitions, as shown here, the rotational selection rules are ΔJ = 0, ±1, $\Delta K_a = \pm 1$, and $\Delta K_c = \pm 1$.

To assign the fundamental transitions of the ν_1 band, we use the same fitting procedure in PGOPHER as that used for ν_6 (described above). The rotational constants and distortion constants are shown in Table I. In addition, Fig. 3 shows the overall simulation spectrum compared to the experimental spectrum, with the residual plot at the bottom of Fig. 3 showing good agreement between the experiment and simulation. There is a less intensity mismatch for this simulation, suggesting that the overall simulation has captured most of the possible transitions. Once again, due to pressure broadening, each peak is a combination of many transitions, each with a different J and K_c, but with the same K_a transition.

Just like for the ν_6 band, the ν_1 band exhibits additional transitions in each stack of peaks. Once again, these progressions can be attributed to hot bands of $1^1_0 4^n_n$ (where n ≤ 4) due to ν_4 (v > 0) population at room temperature. However, for the lower frequency ν_1 band, only transitions up to v = 4 are consistently detectable for the excited ν_4 (v > 0) states, and these excited transitions converge into one peak at lower K_a values unlike in the ν_6 band [as seen in Fig. 3(a)]. The experimentally determined rotational constants for these $1^1_0 4^n_n$ transitions are included in Table III. As with the ν_6 band, we can again determine the vibrational anharmonicity and cross-anharmonicity constants (x_{11} and x_{14}) using the available information and ground state differences. Using the information in Tables I and III, x_{11} was determined to be −0.009(4) cm^{-1} and x_{14} was determined to be 0.049(2) cm^{-1}. The x_{11} anharmonicity constant being close to zero, compared to x_{66} being more negative, is expected for symmetric vs antisymmetric stretching vibrations.

For both ν_6 and ν_1 (across all included hot band transitions), there is a difference in the degree of uncertainty for some of the experimentally determined rotational constants. For example, the origins for ν_6 (v = 1) and ν_1 (v = 1) differ in uncertainty by a factor of 10, with the ν_1 constant being the more accurate value, which is why it is reported with more significant figures. This is mainly due to how the PGOPHER line-fitting procedure calculates the uncertainties given in Tables I and III. When undergoing the line-fitting procedure, the uncertainty in a constant is the calculated standard deviation based on the quality of the fit, and this will necessarily be impacted by the number of transitions included in the fitting procedure. In addition, as more peaks are incorporated into the fit from higher K_a transitions in the ν_6 band compared to the ν_1 band, higher level distortion constants need to be included in the simulation to ensure that these peaks match the experimental spectrum, and not including these constants (as is the case here) means the quality of the fit for the origin constant, and other rotational constants, will have a higher uncertainty.

C. Pressure broadening

The expected Doppler broadening for the observed transitions at room temperature is ~0.0023 cm^{-1}. The instrument line shape function is a Lorentzian with a full-width-at-half-maximum of 0.0142 cm^{-1} (see the supplementary material, Sec. A, for instrument line shape function discussion). When using the instrument

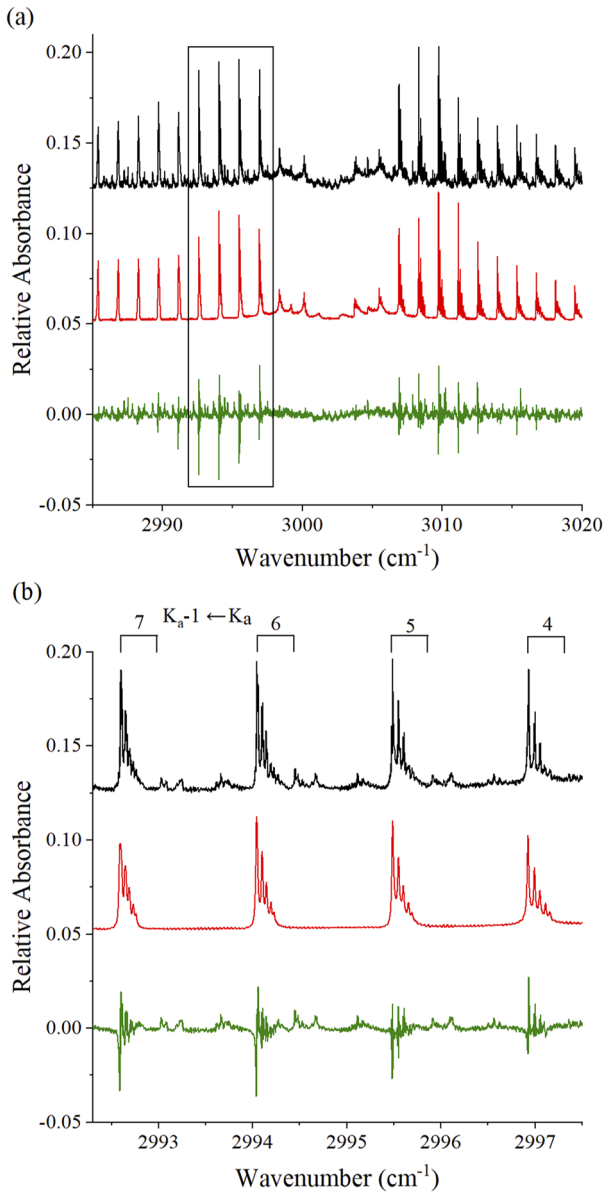

FIG. 3. (a) Comparison of the experimental spectrum (black) and the overall simulation (red), as determined in PGOPHER, for the ν_1 band from 2985 to 3018 cm^{-1}. The overall simulation is the combination of different simulated transitions: fundamental 1^1_0 band and the $1^1_0\,4^n_n$ hot bands, where $n \leq 4$. The y-axis shows relative absorbance between the experimental and simulation spectra, where the simulation has been scaled up to match the experimental. The green line is the residual plot of the experimental minus the overall simulation. (b) Zoomed-in portion of the three spectra, from 2993.4 to 2997.5 cm^{-1}, showing four different K_a transitions in the ^PQ branch.

broadening as the Lorentzian contribution to the linewidth in PGOPHER alongside the expected Doppler broadening as the Gaussian contribution to the linewidth, the experimental spectrum shows additional broadening not captured by the PGOPHER simulation. The remainder of the linewidth is most likely due to pressure broadening.[65–67] This hypothesis is further confirmed by a comparison of the spectrum in this work to that in HITRAN, reported at atmospheric pressure and temperature.[17,22] As previously mentioned, the spectra observed under atmospheric pressure show broad, asymmetric peaks, whereas we observe peak progressions. A comparison is shown in the supplementary material, Fig. C1.

For the pressure broadening studies performed here, the spectra were collected over the 3052–3070 cm^{-1} window, within the ν_6 band, for two different bath gases. From this window, the contour fitting procedure within the PGOPHER program was used to fit an overall Lorentzian broadening parameter (as a full-width-at-half-maximum, FWHM) between 3056.5 to 3069 cm^{-1}, which incorporated 51 peaks across nine different K_a transitions within the ν_6 band. The total Lorentzian broadening parameter includes a contribution from the instrument line shape function, so this is removed prior to the analysis of the pressure broadening contribution. The remaining FWHM is then converted to a half-width-at-half-maximum (HWHM) for the analysis described below. This spectral region was chosen as it has some of the highest intensity peaks and well-defined $6^1_0 4^n_n$ transitions. For each bath gas, the contribution to the overall Lorentzian broadening can be split into two components,

$$\Gamma_{broadening} = p_1 \times b_{self} + p_2 \times b_X, \quad (1)$$

where b_{self} is the self-broadening parameter for CH_2I_2, b_X is the broadening parameter for each broadening gas (X = N_2 or Ar), and p_1 and p_2 are the partial pressures of the respective gases. Attempts were made to separate pressure broadening coefficients as a function of $6^1_0 4^n_n$ vibrational transition and as a function of K_a, but because of the congested spectrum, quantitative results were difficult to obtain for all datasets present, particularly those at higher pressures (>50 mbar). At reduced pressures (<50 mbar), it was found that differences in the pressure broadening coefficients as a function of $6^1_0 4^n_n$ vibrational transition and as a function of K_a were within the uncertainty of the fit.

The concentration of CH_2I_2 unfortunately slightly varies for each total pressure due to experimental conditions. However, as we did not systematically vary the CH_2I_2 concentration, b_{self} was not determined in this work, but rather the contribution of self-broadening to the overall pressure broadening at a specific CH_2I_2 partial pressure. Since the CH_2I_2 concentration changes between 0.003 and 0.05 mbar for both N_2 and Ar (keeping an average of 0.01% CH_2I_2 in the gas mix), this variance must be removed from each overall Lorentzian broadening parameter in order to accurately determine the broadening coefficient for each bath gas (b_X) without the influence of changing self-broadening parameters. This process required fitting a line to an initial plot of $\Gamma_{broadening}$ vs N_2 or Ar partial pressure (from 20 to 1000 mbar), where the intercept from the fit (for each gas) represents the average self-broadening parameter. This average self-broadening value is used to correct for differences of CH_2I_2 concentrations from the average CH_2I_2 concentration. The self-broadening contribution is then removed from the overall Lorentzian half-width-at-half-maximum, $\Gamma_{boadening}$.[68] This new Lorentzian value can be re-plotted against the partial pressure of N_2 or Ar, and a line fit of this plot will give a slope corresponding to the broadening coefficient of either N_2 or Ar. The final results can

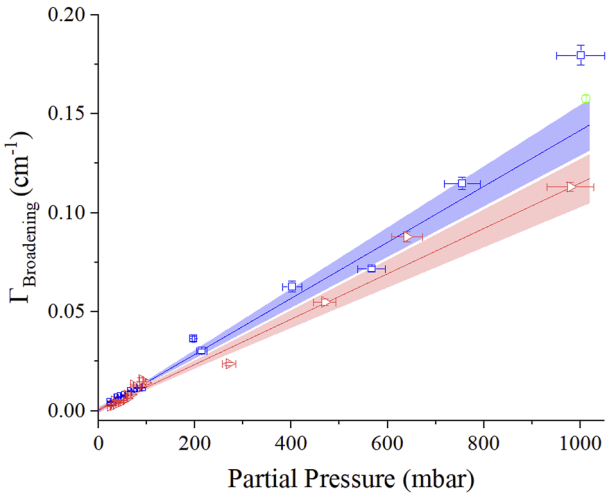

FIG. 4. Blue squares are the N_2 data with the corresponding blue linear line fit and 95% confidence limits, and the argon data are in red triangles, with its corresponding red linear line fit and 95% confidence limits. The reference data available from HITRAN have been included (green circle).

TABLE IV. Pressure broadening coefficients of CH_2I_2 by N_2 and Ar.

Collision partner	b (cm^{-1} atm^{-1})
Ar	0.116 (6)
N_2	0.143 (6)

be seen in Fig. 4. Note that correcting for differences in CH_2I_2 concentrations (and, thus, self-broadening contributions) did not make a significant difference to the final corrected results, which were still within the error of the initial uncorrected analysis, likely because the fraction of CH_2I_2 in the mix (0.01%) was significantly smaller than the bath gas.

The first bath gas chosen was N_2 at a range of pressures from 25 to 1000 mbar. After correcting for differences in the CH_2I_2 concentration, the $\Gamma_{broadening}$ parameter ranged from 0.003 cm^{-1} at 26.3 mbar to 0.18 cm^{-1} at 1000 mbar. To determine the N_2 broadening contribution, the data were fitted to a line (Fig. 4) with a slope representing the N_2 broadening coefficient of 1.41(6) $\times$ 10^{-4} cm^{-1} $mbar^{-1}$ or 0.143(6) cm^{-1} atm^{-1} (Table IV). The second bath gas chosen was argon at a range of pressures from 24 to 980 mbar. After the correction of the CH_2I_2 concentration, the $\Gamma_{broadening}$ parameter ranged from 0.003 cm^{-1} at 24.0 mbar to 0.11 cm^{-1} at 980 mbar. To determine the Ar broadening contribution, the data were fitted to a line (Fig. 4) with a slope representing the Ar broadening coefficient of 1.14(6) $\times$ 10^{-4} cm^{-1} $mbar^{-1}$ or 0.116(6) cm^{-1} atm^{-1} (Table IV). Discussion of the pressure broadening results is shown in Sec. IV C.

D. Anharmonic calculations

In order to confirm the observed experimental spectrum and our hypothesis for the observed progressions being due to hot bands, calculations were performed to determine anharmonic frequencies and rotational constants. There are not many basis sets that can be used for molecules involving iodine, so two suitable basis sets were chosen for the anharmonic calculations of the transition frequencies and the rotational constants: Def2QZVPP[69] and MIDIX.[70] Several levels of theory that have been shown to work with iodine-containing molecules were also used (see the supplementary material, Sec. D) and generally agreed with the overall shape of the experiment spectrum. However, the wB97X/Def2QZVPP results agreed the best with the experimental spectrum (Fig. 5), so the level of theory is used in this discussion. A semi-empirical method was used to simulate the spectra based on the computational results in PGOPHER, which involved determining the difference between the calculated upper and lower state rotational constants for the appropriate vibrational levels (Δ_i) and then applying that Δ_i value to the experimental rotational constants determined via microwave spectroscopy.[15] This methodology was recently used for the analysis of the CH_2Br_2 vibrational spectrum.[43] The vibrational origins for the

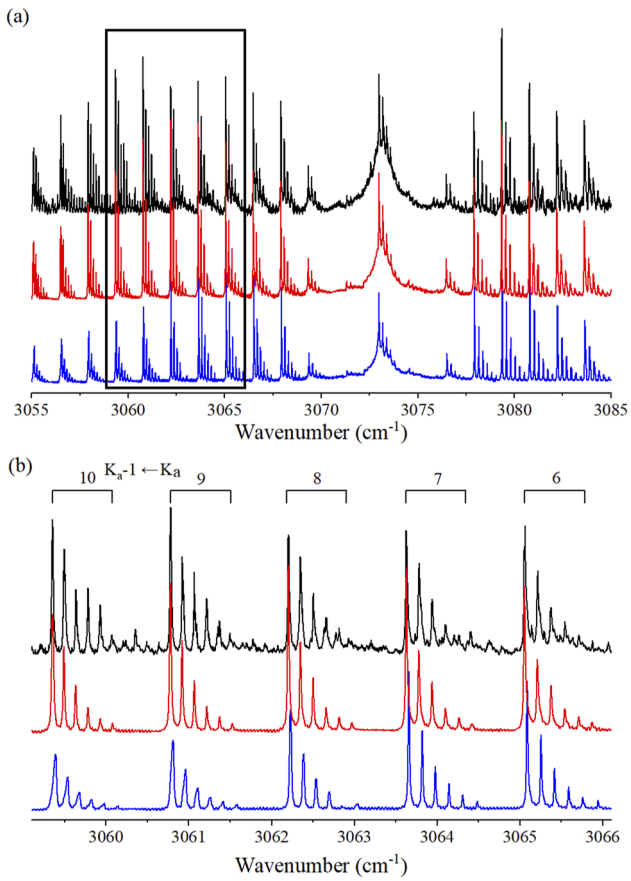

FIG. 5. Comparison of the experimental spectrum (black), the line-fitted simulation (red), and the semi-empirical simulation based on the results of the wB97X/Def2QZVPP calculations (blue). (a) Sub-section of all three spectra, from 3055 to 3085 cm^{-1}, covering the 6^1_0 band (including the 6^1_0 4^n_n transitions where $n \leq 5$). (b) Zoomed-in portion of the three spectra, from 3059.1 to 3066.1 cm^{-1}, showing five different K_a transitions in the ^PQ branch.

TABLE V. Comparison of the calculated and experimentally determined anharmonic frequencies and rotational constants for CH_2I_2 for the vibrational ground state (v = 0), ν_6 (v = 1), ν_4 (v = 1), and the first hot band ν_6 (v = 1) + ν_4 (v = 1). All values are given in cm^{-1}, and error bars for experimental values are given above in Table I.

		Ground state (v = 0)	ν_6 (v = 1)	$\Delta_i/10^{-6}$	ν_4 (v = 1)	ν_6 (v = 1) + ν_4 (v = 1)	$\Delta_j/10^{-6}$
wB97X/Def2QZVPP	ν	0	3196.503	⋯	122.8	3319.646 0	⋯
	A	0.756 904	0.754 001	−46.3	0.758 381	0.758 335	−46.0
	B	0.020 722	0.020 723	0.9	0.020 741	0.020 742	1.0
	C	0.020 248	0.020 250	1.2	0.020 265	0.020 266	1.0
Experimental	ν	0	3072.906	⋯	121.0	3194.093 6	⋯
	A	0.734 994[a]	0.735 500	9.8	0.737 856[a]	0.737 784	−70.1
	B	0.020 700[a]	0.207 014	1.3	0.020 694[a]	0.020 696	2.5
	C	0.020 206[a]	0.020 208	1.5	0.020 198[a]	0.020 201	2.5

[a]Constants from Ref. 15.

semi-empirical spectra were also changed to best match the experimental data. See Table V for the calculated rotational constants and Δ_i values. Further calculated rotational constants for ν_6 (v = 1) + ν_4 (v ≤ 5) can be found in the supplementary material, Sec. D. For all simulations, the only constants that were changed between the lower and upper states were the A, B, and C rotational constants; all higher order constants included in the simulations were held constant, as determined from the microwave data. Further results for both ν_1 and ν_6 bands, including hot band transitions, can also be found in the supplementary material, Sec. D. Vibrational information from calculations is collated in Table D4 of the supplementary material.

IV. DISCUSSION

A. Additional peaks

As visible in Figs. 2 and 3, there are some low intensity peaks between progressions that the simulations, for both the ν_6 and ν_1 bands, have not incorporated. This is particularly visible in Fig. 3(b), where there are multiple peaks near 2993.3, 2994.5, and 2996.0 cm^{-1}. There are a few options as to why these small peaks have not been captured by the simulation. First, the peaks could be from something other than CH_2I_2 or from CH_2I_2 dimers. We confirmed that the presence of these peaks is dependent on CH_2I_2 being present. CH_2I_2 dimers have been calculated to be stable by ~4 kcal mol^{-1} (1400 cm^{-1}), so it is possible that these dimers exist in our sample.[34] Using the region from 3050 to 3070 cm^{-1}, we investigated the appearance of the spectra as a function of CH_2I_2 concentration, total pressure, and bath gas identity. Keeping the concentration of CH_2I_2 constant, relative intensities of these small peaks compared to the peaks captured by the simulation are independent of pressure over the range of 20 mbar–200 mbar and independent of the bath gas (Ar or N_2). Using just the Ar spectra, increasing the relative amount of CH_2I_2 in the sample from 0.1% to 10% (while keeping the same total pressure) did not change the relative intensities of the small peaks compared to the peaks captured by the simulation. These tests indicate that it is highly unlikely that CH_2I_2 dimers are responsible for these peaks, especially since any dimers formed would be in such low abundance compared to the monomers in the gaseous sample.

Given that the peaks are dependent on CH_2I_2 and are unlikely to be due to dimers, they are, therefore, most probably caused by overtones, combination bands, or other hot band transitions as already seen with the ν_4 bands. There are no straightforward combinations of other vibrational normal modes as either combination bands or overtones that result in peaks in this spectral region. As the current simulations show there is population in up to the ν_4 (v = 5) state, which has a transition frequency of ~605 cm^{-1}, other vibrational modes of CH_2I_2 can have population in excited vibrational states, specifically the ν_3 (v = 1) state at 493.01 cm^{-1} and the ν_9 (v = 1) state at 584.21 cm^{-1}.[19] However, the lack of microwave or infrared data for these states means the ability to simulate these peaks would come with a large degree of uncertainty, especially given the small peak intensity and the congested nature of the spectrum. Performing further anharmonic calculations, using the wB97X/Def2QZVPP method and basis set, we calculated the rotational constants of the ν_3 (v = 1) and ν_9 (v = 1) states and the corresponding hot band with ν_6 and ν_1. Although further simulations proved that the $6^1_0 3^1_1$ and $6^1_0 9^1_1$ transitions would be possible if there was initial population in ν_3 (v = 1) and ν_9 (v = 1), the uncertainty within the calculations precludes robust peak assignment and meaningful spectral fitting.

B. Determining systemic uncertainty

Due to the low vapor pressure of CH_2I_2, we heated the sample to increase the vapor pressure and ensure a larger concentration of CH_2I_2 in the flow cell. However, there are several sources of systematic error with this method. First, a water bath (313 K) was used to heat the sample container, which is a Teflon-lined stainless steel container. Because Teflon is not an effective thermal conductor, the water bath temperature is not an accurate reflection of the temperature of the CH_2I_2 liquid sample. Second, the distance between the sample cup and the flow cell is ~2 m of Teflon tubing, so there is a high probability of sample loss to walls. Assuming no sample sticks to the tubing and we know the temperature of the liquid sample, the concentration of CH_2I_2 in the cell would be (2.29 ± 0.05) × 10^{16} molecule cm^{-3}, and we could report our spectrum as absorption cross section as a function of wavenumber. However, a comparison to the reported absorption cross section spectrum available in HITRAN[17] shows a factor of ~3.7 difference between the integrated absorption cross section over 2965.1–3025.0 cm^{-1}: 1.81 × 10^{-20} cm^2 $molecule^{-1}$ for our work and 6.74 × 10^{-20} cm^2 $molecule^{-1}$ for the reference spectrum. In addition, from 2936.3 to 3125.4 cm^{-1} (the full spectrum), the factor is increased to 4.5, with our work giving a total integrated

absorption cross section of 1.08×10^{-19} cm^2 molecule^{-1} and 4.87×10^{-19} cm^2 molecule^{-1}. This difference in these two factors can be attributed to a combination of water impurity peaks across the whole experimental spectrum (see the red asterisks in Fig. 1, for example), some negative absorption values that occur in the baseline of our spectrum, and uncertainty in possible water contents of the reference spectrum.

For the reference data,[17] care was taken to develop a delivery method that ensured little to no sample was lost between a syringe pump and the white cell used in the measurement.[71] This method involved heating the connecting parts, using a disseminator head, and demonstrated a less than 1% difference between the calculated and measured concentrations for 2-propanol. Therefore, the reported absorption cross section for the reference data can be considered highly accurate. Since the interaction path length in our Herriott cell is known to a high level of uncertainty, determined through analysis of a known methane sample, the difference here is most likely due to uncertainty in the concentration of CH_2I_2 in the flow cell. If we use the average of the two factors reported above (3.7 and 4.5) between the reported numerical integrated area and the numerical integrated area of our spectrum, and corrected our experimental CH_2I_2 concentration, the CH_2I_2 concentration in our absorption cell would have a lower limit of $(6.8 \pm 1.3) \times 10^{15}$ molecule cm^{-3}. The uncertainty in temperature of the liquid sample alone does not account for this close to fourfold difference, so a combination of both wall-loss and temperature are likely the contributing factors to this discrepancy. Thus, the right y-axis (absorption cross section in cm^2 molecule^{-1}) for the data reported in Fig. 1 has been corrected for the systematic over-prediction of the CH_2I_2 concentration, with the error determined from the error in the concentration and the error in the cell path length. Future studies implement an improved delivery method to avoid this systematic uncertainty moving forward.

C. Comparison of pressure broadening studies

First, we can make comparisons in the broadening coefficients between N_2 (b_{N2}) = 0.143(6) cm^{-1} atm^{-1} and argon (b_{Ar}) = 0.116(6) cm^{-1} atm^{-1}. These are of similar magnitude but different in value and are just outside the margins of error to be considered the same value. Out of the two coefficients, b_{Ar} is the smaller value, meaning that collisions with nitrogen result in ~1.25 times broader CH_2I_2 transitions, which will impact atmospheric observations of CH_2I_2 vibrational spectra. However, a comparison of the b_{N2} coefficient with similar molecules shows our work to perhaps be higher than expected. While there are a lack of pressure broadening studies for CH_2Cl_2 and CH_2Br_2, CH_2F_2 has an abundance of studies where most recently, the J-dependent b_{N2} parameter was shown to range from 0.061 to 0.125 cm^{-1} atm^{-1}, with an average value of 0.087 cm^{-1} atm^{-1}.[68] In addition, there have been a plethora of studies on CH_3X molecules, where X = F, Cl, Br, or I, which all reported b_{N2} coefficients close to 0.105(3) cm^{-1} atm^{-1}. Using an average and standard deviation from a range of reported data, the N_2 broadening coefficients are CH_3F 0.101(10) cm^{-1} atm^{-1},[72] CH_3Cl 0.108(12) cm^{-1} atm^{-1},[73] CH_3Br 0.103(11) cm^{-1} atm^{-1},[74] and CH_3I 0.107(14) cm^{-1} atm^{-1}.[75] We should note that these are averages over the J-dependent values of the N_2 broadening coefficient. In the case of CH_3I, the J-dependent b_{N2} values ranged from 0.072(2) cm^{-1} atm^{-1} to 0.148(4) cm^{-1} atm^{-1}. While our value at 0.143(6) cm^{-1} atm^{-1} is higher than the average b_{N2} coefficients, it is within the upper range of the J-dependent broadening coefficient for CH_3I. Unfortunately, there is even less information surrounding Ar broadening coefficients; however, one study[76] reported b_{Ar} values for CH_3F (as a function of J) ranging from 0.050(3) cm^{-1} atm^{-1} to 0.080(5) cm^{-1} atm^{-1}, which is significantly less than the reported b_{N2} as stated above. Assuming CH_2I_2 follows the same trend, our b_{Ar} being a lower value than b_{N2} can be assumed to be correct. However, if we were over-predicting the N_2 broadening contribution, we could be underpredicting the contribution from another factor, namely, the CH_2I_2 self-broadening coefficient or the instrument line shape function. If the instrument line shape function or self-broadening coefficient were underpredicted, then our b_{Ar} measurement would also be over-predicted.

We can also make comparisons in the overall Lorentzian broadening parameters for this work and the reference spectrum as this study uses N_2 as the bath gas at atmospheric pressure (1013 mbar). Determined through the same contour fitting method used for this work, the $\Gamma_{broadening}$ for the reference data is found to be 0.158 cm^{-1}. Extrapolating the linear fit to our broadening coefficient as a function of pressure, we calculate a $\Gamma_{broadening}$ value of 0.14 ± 0.01 cm^{-1} at the same pressure (1013 mbar). However, the $\Gamma_{broadening}$ value for the reference data still includes the instrument line shape function (not reported) and does not account for the difference in CH_2I_2 concentrations between samples, which could account for the differences seen here.

D. Comparison of anharmonic calculations

To refrain from repetitive analysis, this section will focus on the comparison between the wB97X/Def2QZVPP calculations and the experimental spectrum, specifically for the 6^1_0 transition. This calculation was chosen for comparative analysis as it is most similar to the spectrum presented in this work, although other levels of theory were also consistent with our interpretation of the experimental spectrum (see the supplementary material, Sec. D). Looking initially at Table V, it is obvious that the calculated rotational constants for the ground state (v = 0) and ν_6 (v = 1) are different from the microwave determined ground state constants and the experimentally determined ν_6 (v = 1) constants. However, the difference between the ground state and the first excited state is a better comparison, with the B and C rotational constants having very similar Δ_i values, but the A constant has a large difference, 9.8×10^{-6} for this work and -46.3×10^{-6} for the wB97X/Def2QZVPP calculation. On inspection of the simulations (Fig. 5), this difference in the Δ_A between this work and the calculation does not make a large visible difference. The general shape of each peak is well matched, with the only discernible difference being the peak locations, which is due to the difference in the Δ_A values. In addition, the relative intensity pattern of the peaks differs between the experimental spectrum, the line-fitted simulation, and the semi-empirical simulation. A further comparison between the calculated integrated intensities (km mol^{-1}) for ν_6 and ν_1 show a band strength ratio of 1:0.39 for ν_6:ν_1, which agrees fairly well with the experimental ratio of 1:0.23, despite the calculation not including contributions from the $1^1_0 4^n_n$ and $6^1_0 4^n_n$ transitions for n > 0.

Alongside performing calculations for the 6^1_0 band, we also calculated rotational constants for the $6^1_0\ 4^n_n$ transition, where n ≤ 5.

The Δ_j values for the first hot band (where n = 1) are almost half the value compared to the fitted experimental data. However, once again, this difference in Δ_j does not massively impact the overall semi-empirical simulation, and we do observe transitions associated with the $6^1_0\,4^n_n$ hot band, which further validates the experimentally observed rotational constants and confirms that the hot band analysis presented here is a reasonable hypothesis for the observed peak progressions.

E. Comparison with other CH_2X_2 compounds

With the addition of the ν_4 hot bands to the CH_2I_2 spectrum, it is reasonable to assume that other CH_2X_2 (where X = F, Cl, or Br) may exhibit the same phenomenon at room temperature. The 4^1_0 transition frequencies for each dihalomethane are CH_2F_2 ν_4 = 528 cm^{-1},[38] CH_2Cl_2 ν_4 = 281.5 cm^{-1},[40] CH_2Br_2 ν_4 = 169 cm^{-1},[42] and CH_2I_2 ν_4 = 121 cm^{-1}.[17] It is expected that CH_2Br_2 would exhibit the same hot bands, but CH_2Cl_2 and CH_2F_2 would display little to none of these transitions under room temperature conditions. Focusing on CH_2Br_2, we can compare the population ratios for CH_2I_2 and CH_2Br_2 at room temperature for $v \le 4$, assuming a Boltzmann distribution of the population. Fixing the fundamental transition to a value of 1, all the subsequent ratios are relative to this value: CH_2I_2, 1:0.56:0.32:0.18:0.10, and CH_2Br_2, 1:0.43:0.18:0.08:0.03. As these ratios are not so different from each other, it is highly probable that for CH_2Br_2, up to v = 3 for the hot band should be visible in a high-resolution, room temperature spectrum for both ν_1 and ν_6. However, despite the population ratios predicting hot bands for CH_2Br_2, the experimental high-resolution spectrum and corresponding simulation[43] do not take these transitions into account. The explanation for the additional peaks were attributed to the three isotopologs of CH_2Br_2 ($CH_2{}^{79}Br{}^{79}Br$, $CH_2{}^{79}Br{}^{81}Br$, and $CH_2{}^{81}Br{}^{81}Br$). While this assumption is reasonable, the experimental frequencies and rotational constants are far from the calculated values, and the relative intensities of the progressions do not match the isotopic abundance ratios of the molecules. Current collaborative work is ongoing to take any hot band transitions into account in the interpretation of the CH_2Br_2 spectrum.

Despite this lack of hot band structure for CH_2Cl_2 and CH_2F_2, their mid-IR vibrational spectra show other interacting vibrational transitions that do not appear in the corresponding spectra for CH_2Br_2 and CH_2I_2. For example, CH_2F_2 shows medium intensity overtone bands, $2\nu_2$ centered at 3026.23 cm^{-1}, and $2\nu_8$ at 2838.64 cm^{-1}, alongside ν_1 at 2947.9 cm^{-1} and ν_6 at 3014.45 cm^{-1}. CH_2Cl_2 exhibits two overtone bands, $2\nu_2$ and $2\nu_8$, at 2853.66 cm^{-1} and 2526.58 cm^{-1} respectively, which are both somewhat nearby ν_1 at 2997.33 cm^{-1} and ν_6 at 3055 cm^{-1}.[40] As these transitions are close in energy, it is expected that Fermi resonances, Coriolis coupling, and/or Darling–Dennison resonances will affect the observed rovibrational spectra. For CH_2F_2, experiments have demonstrated an a-axis Coriolis interaction between the $2\nu_2$ and ν_6 bands,[36] and for CH_2Cl_2, literature has reported Fermi resonances between ν_1 and $2\nu_8$ bands, and ν_1 and $2\nu_2$ bands alongside Darling–Dennison resonances between $2\nu_1$ and $2\nu_6$, and $2\nu_2$ and $2\nu_8$.[40]

The same transitions for CH_2I_2 are much lower in wavenumber than ν_1 and ν_6, with $2\nu_2$ predicted near 2747 cm^{-1} (not seen in the literature or in attempts with our experimental apparatus, potentially a very weak transition) and $2\nu_8$ at 2222.42 cm^{-1}.[17] As the overtone bands of ν_2 and ν_8 are at a much lower frequency than the other three transitions, we do not expect any coupling or resonances with this band from either ν_1, ν_6, or $2\nu_2$. Furthermore, the lack of evidence for $2\nu_2$ in the gas phase suggests there would be little to no coupling or resonances to enhance the intensity of this band.

VI. CONCLUSION

Using direct frequency comb spectroscopy, we have presented the high-resolution, rotationally resolved vibrational spectrum of CH_2I_2 2960–3125 cm^{-1}. Under the lower pressure (11 mbar) conditions in the current work, an abundance of peaks are observed over this wavenumber range. The experimental spectrum incorporates both the ν_1 and ν_6 vibrational bands of CH_2I_2, and we have reported the v = 1 rotational constants for both the bands. In addition, we have shown that initial population in the ν_4 ICI bending mode was the cause for the progressions observed in each spectrum. These hot band transitions have been simulated, and rotational constants have been determined for both the bands, for $6^1_0\,4^n_n$ ($n \le 5$) and $1^1_0\,4^n_n$ ($n \le 4$). The next step for this work is to a record a low temperature (<10 K) rovibrational spectrum of CH_2I_2, which would help confirm our hot band analysis and allow for more accurate rotational constants. This work is currently under way using molecular beam apparatus. We also report pressure broadening coefficients for CH_2I_2 with Ar and N_2, which are somewhat higher than expected. However, we are able to extrapolate our broadening coefficient findings to the atmospheric pressure spectrum previously reported. The detailed analysis of this lower pressure spectrum could be useful for atmospheric detection of CH_2I_2 by infrared spectroscopy when sampling air into low pressure absorption cells. There is almost an order of magnitude intensity increase in the observed peaks in the low pressure spectrum compared to an atmospheric pressure spectrum, simply due to narrowing spectroscopic transitions by reducing pressure broadening, which impacts the sensitivity with which CH_2I_2 could be monitored using infrared spectroscopy.

SUPPLEMENTARY MATERIAL

See the supplementary material for additional information on the instrument line shape function, a breakdown of the full rovibrational simulation, a comparison to the HITRAN reference spectrum, further information on the computational results, and a discussion of the 4^n_0 band origins.

ACKNOWLEDGMENTS

This work was supported by funding from the EPSRC (Grant Nos. EP/R01518X/1 and EP/R513258/1). Part of this work was undertaken on ARC3, part of the High Performance Computing facilities at the University of Leeds, UK. The authors thank Professor Colin Western (University of Bristol) and Dr. Ibrahim [Leibniz Institute for Plasma Science and Technology (INP)].

AUTHOR DECLARATIONS

Conflict of Interest

The authors have no conflicts to disclose.

DATA AVAILABILITY

The data that support the findings of this study are openly available in The Research Data Leeds repository at https://doi.org/10.5518/1083. Data in this repository include the experimental spectrum, PGOPHER simulation, PGOPHER generated line lists, and Gaussian output files for the computational results.

REFERENCES

[1] C. E. Jones, K. E. Hornsby, R. Sommariva, R. M. Dunk, R. von Glasow, G. McFiggans, and L. J. Carpenter, Geophys. Res. Lett. **37**(18), L18804, https://doi.org/10.1029/2010gl043990 (2010).
[2] Y. Yokouchi, T. Saito, A. Ooki, and H. Mukai, J. Geophys. Res.: Atmos. **116**, 10, https://doi.org/10.1029/2010jd015252 (2011).
[3] S. M. Ball, A. M. Hollingsworth, J. Humbles, C. Leblanc, P. Potin, and G. McFiggans, Atmos. Chem. Phys. **10**(13), 6237 (2010).
[4] T. K. Koenig, S. Baidar, P. Campuzano-Jost, C. A. Cuevas, B. Dix, R. P. Fernandez, H. Guo, S. R. Hall, D. Kinnison, B. A. Nault, K. Ullmann, J. L. Jimenez, A. Saiz-Lopez, and R. Volkamer, Proc. Natl. Acad. Sci. U. S. A. **117**(4), 1860 (2020).
[5] A. Saiz-Lopez, R. P. Fernandez, C. Ordóñez, D. E. Kinnison, J. C. Gómez Martín, J.-F. Lamarque, and S. Tilmes, Atmos. Chem. Phys. **14**(23), 13119 (2014).
[6] A. Saiz-Lopez, J. M. C. Plane, A. R. Baker, L. J. Carpenter, R. von Glasow, J. C. Gómez Martín, G. McFiggans, and R. W. Saunders, Chem. Rev. **112**(3), 1773 (2012).
[7] J. C. Mössinger, D. E. Shallcross, and R. Anthony Cox, J. Chem. Soc., Faraday Trans. **94**(10), 1391 (1998).
[8] J. G. Calvert and S. E. Lindberg, Atmos. Environ. **38**(30), 5087 (2004).
[9] J. L. Jimenez, R. Bahreini, D. R. Cocker, H. Zhuang, V. Varutbangkul, R. C. Flagan, J. H. Seinfeld, C. D. O'Dowd, and T. Hoffmann, J. Geophys. Res.: Atmos. **108**(D10), 4318, https://doi.org/10.1029/2002JD002452 (2003).
[10] T. J. Dillon, M. E. Tucceri, R. Sander, and J. N. Crowley, Phys. Chem. Chem. Phys. **10**(11), 1540 (2008).
[11] O. Welz, J. D. Savee, D. L. Osborn, S. S. Vasu, C. J. Percival, D. E. Shallcross, and C. A. Taatjes, Science **335**(6065), 204 (2012).
[12] A. Mandal, P. J. Singh, A. Shastri, and B. N. Jagatap, J. Chem. Phys. **140**(19), 194312 (2014).
[13] M. Ito, P.-k. C. Huang, and E. M. Kosower, Trans. Faraday Soc. **57**, 1662 (1961).
[14] S. L. Baughcum and S. R. Leone, J. Chem. Phys. **72**(12), 6531 (1980).
[15] Z. Kisiel, E. Białkowska-Jaworska, and L. Pszczółkowski, J. Mol. Spectrosc. **199**(1), 5 (2000).
[16] Z. Kisiel, L. Pszczolkowski, W. Caminati, and P. G. Favero, J. Chem. Phys. **105**(5), 1778 (1996).
[17] T. J. Johnson, T. Masiello, and S. W. Sharpe, Atmos. Chem. Phys. **6**, 2581 (2006).
[18] T. A. Ford, J. Mol. Spectrosc. **58**(2), 185 (1975).
[19] S. W. Sharpe, T. J. Johnson, R. L. Sams, P. M. Chu, G. C. Rhoderick, and P. A. Johnson, Appl. Spectrosc. **58**(12), 1452 (2004).
[20] F. L. Voelz, F. F. Cleveland, A. G. Meister, and R. B. Bernstein, J. Opt. Soc. Am. **43**(11), 1061 (1953).
[21] E. K. Plyler and W. S. Benedict, J. Res. Natl. Bur. Stand. **47**(3), 202 (1951).
[22] I. E. Gordon, L. S. Rothman, R. J. Hargreaves, R. Hashemi, E. V. Karlovets, F. M. Skinner, E. K. Conway, C. Hill, R. V. Kochanov, Y. Tan, P. Wcisło, A. A. Finenko, K. Nelson, P. F. Bernath, M. Birk, V. Boudon, A. Campargue, K. V. Chance, A. Coustenis, B. J. Drouin, J. M. Flaud, R. R. Gamache, J. T. Hodges, D. Jacquemart, E. J. Mlawer, A. V. Nikitin, V. I. Perevalov, M. Rotger, J. Tennyson, G. C. Toon, H. Tran, V. G. Tyuterev, E. M. Adkins, A. Baker, A. Barbe, E. Canè, A. G. Császár, A. Dudaryonok, O. Egorov, A. J. Fleisher, H. Fleurbaey, A. Foltynowicz, T. Furtenbacher, J. J. Harrison, J. M. Hartmann, V. M. Horneman, X. Huang, T. Karman, J. Karns, S. Kassi, I. Kleiner, V. Kofman, F. Kwabia–Tchana, N. N. Lavrentieva, T. J. Lee, D. A. Long, A. A. Lukashevskaya, O. M. Lyulin, V. Y. Makhnev, W. Matt, S. T. Massie, M. Melosso, S. N. Mikhailenko, D. Mondelain, H. S. P. Müller, O. V. Naumenko, A. Perrin, O. L. Polyansky, E. Raddaoui, P. L. Raston, Z. D. Reed, M. Rey, C. Richard, R. Tóbiás, I. Sadiek, D. W. Schwenke, E. Starikova, K. Sung, F. Tamassia, S. A. Tashkun, J. Vander Auwera, I. A. Vasilenko, A. A. Vigasin, G. L. Villanueva, B. Vispoel, G. Wagner, A. Yachmenev, and S. N. Yurchenko, J. Quant. Spectrosc. Radiat. Transfer **277**, 107949 (2022).
[23] J. Orphal, N. Ibrahim, and C. E. Fellow, in 19th Colloquium on High Resolution Molecular Spectroscopy, Salamanca, Spain, 2005.
[24] M. Satta, P. Bolognesi, A. Cartoni, A. R. Casavola, D. Catone, P. Markus, and L. Avaldi, J. Chem. Phys. **143**(24), 244312 (2015).
[25] R. Walllace and A. A. Wu, Chem. Phys. **39**(2), 221 (1979).
[26] C. G. Elles, D. Bingemann, M. M. Heckscher, and F. F. Crim, J. Chem. Phys. **118**(12), 5587 (2003).
[27] D. Bingemann, A. M. King, and F. F. Crim, J. Chem. Phys. **113**(12), 5018 (2000).
[28] W. M. Kwok and D. L. Phillips, J. Chem. Phys. **104**(7), 2529 (1996).
[29] M. M. Heckscher, L. Sheps, D. Bingemann, and F. F. Crim, J. Chem. Phys. **117**(19), 8917 (2002).
[30] C. M. Cheatum, M. M. Heckscher, D. Bingemann, and F. F. Crim, J. Chem. Phys. **115**(15), 7086 (2001).
[31] V. B. Kartha, J. Mol. Spectrosc. **24**(1), 368 (1967).
[32] M. P. Marzocchi, V. Schettino, and S. Califano, J. Chem. Phys. **45**(5), 1400 (1966).
[33] J. N. Kondo, T. Higashi, H. Yamamoto, M. Hara, K. Domen, and T. Onishi, Surf. Sci. **349**(3), 294 (1996).
[34] L. Almasy and A. Bende, Molecules **24**(9), 1810 (2019).
[35] R. D. Amos, N. C. Handy, W. H. Green, D. Jayatilaka, A. Willetts, and P. Palmieri, J. Chem. Phys. **95**(11), 8323 (1991).
[36] T. J. Cronin, X. Wang, G. A. Bethardy, and D. S. Perry, J. Mol. Spectrosc. **194**(2), 236 (1999).
[37] Q. Gou, L. Spada, M. Vallejo-López, Z. Kisiel, and W. Caminati, Chem. - Asian J. **9**(4), 1032 (2014).
[38] N. Tasinato, G. Regini, P. Stoppa, A. P. Charmet, and A. Gambi, J. Chem. Phys. **136**(21), 214302 (2012).
[39] P. Stoppa, N. Tasinato, A. Baldacci, A. Pietropolli Charmet, S. Giorgianni, F. Tamassia, E. Cané, and M. Villa, J. Quant. Spectrosc. Radiat. Transfer **175**, 8 (2016).
[40] Q.-h. Liu, X.-n. Li, L.-y. Hao, C. Tan, Y.-g. Zhou, P. Chen, and H. Zhu, Chin. J. Chem. Phys. **19**(1), 15 (2006).
[41] T. J. Wallington, B. P. Pivesso, A. M. Lira, J. E. Anderson, C. J. Nielsen, N. H. Andersen, and Ø. Hodnebrog, J. Quant. Spectrosc. Radiat. Transfer **174**, 56 (2016).
[42] R. S. Dennen, E. A. Piotrowski, and F. F. Cleveland, J. Chem. Phys. **49**(10), 4385 (1968).
[43] I. Sadiek and G. Friedrichs, Spectrochim. Acta, Part A **181**, 180 (2017).
[44] M. N. Deo, R. D'Cunha, A. Weber, and W. B. Olson, J. Mol. Spectrosc. **154**(1), 83 (1992).
[45] J. Morcillo, L. J. Zamorano, and J. M. V. Heredia, Spectrochim. Acta **22**(12), 1969 (1966).
[46] G. L. Fox and H. B. Schlegel, J. Chem. Phys. **92**(7), 4351 (1990).
[47] C. W. Brown, R. J. Obremski, J. R. Allkins, and E. R. Lippincott, J. Chem. Phys. **51**(4), 1376 (1969).
[48] G. S. Devendorf, M.-H. A. Hu, and D. Ben-Amotz, J. Phys. Chem. A **102**(52), 10614 (1998).
[49] R. Escribano, J. M. Orza, S. Montero, and C. Domingo, Mol. Phys. **37**(2), 361 (1979).
[50] M. Podsiadło and A. Katrusiak, J. Phys. Chem. B **112**(17), 5355 (2008).
[51] T. Shimanouchi and I. Suzuki, J. Mol. Spectrosc. **8**(1), 222 (1962).
[52] J. F. Bertrán, B. La Serna Torres, D. F. Félix, and B. Lokshin, J. Raman Spectrosc. **19**(1), 33 (1988).
[53] M. Podsiadlo, K. Dziubek, M. Szafranski, and A. Katrusiak, Acta Crystallogr., Sect. B: Struct. Sci., Cryst. Eng. Mater. **B62**, 1090 (2006).
[54] J. L. Duncan, G. D. Nivellini, and F. Tullini, J. Mol. Spectrosc. **118**(1), 145 (1986).
[55] N. Picqué and T. W. Hänsch, Nat. Photonics **13**(3), 146 (2019).
[56] A. Schliesser, N. Picqué, and T. W. Hänsch, Nat. Photonics **6**(7), 440 (2012).
[57] M. L. Weichman, P. B. Changala, J. Ye, Z. Chen, M. Yan, and N. Picqué, J. Mol. Spectrosc. **355**, 66 (2019).
[58] J. H. Lehman and M. L. Weichman, in *Emerging Trends in Chemical Applications of Lasers* (American Chemical Society, 2021), Vol. 1398, p. 61.

[59]F. C. Roberts, H. J. Lewandowski, B. F. Hobson, and J. H. Lehman, Mol. Phys. **118**, e1733116 (2020).
[60]F. Zhu, H. Hundertmark, A. A. Kolomenskii, J. Strohaber, R. Holzwarth, and H. A. Schuessler, Opt. Lett. **38**(13), 2360 (2013).
[61]M. Shirasaki, Fujitsu Sci. Tech. J. **35**(1), 113 (1999).
[62]J. Ye and S. T. Cundiff, *Femtosecond Optical Frequency Comb: Principle, Operation, and Applications* (Springer, New York, UK, 2005).
[63]P. D. C. L. Yaws, *Chemical Properties Handbook* (McGraw-Hill Education, New York, 1999).
[64]C. M. Western, J. Quant. Spectrosc. Radiat. Transfer **186**, 221 (2017).
[65]G. Peach, Adv. Phys. **30**(3), 367 (1981).
[66]H. Rabitz, Annu. Rev. Phys. Chem. **25**(1), 155 (1974).
[67]C. J. Tsao and B. Curnutte, J. Quant. Spectrosc. Radiat. Transfer **2**(1), 41 (1962).
[68]N. Tasinato, A. Turchetto, C. Puzzarini, P. Stoppa, A. P. Charmet, and S. Giorgianni, Mol. Phys. **112**(18), 2384 (2014).
[69]F. Weigend and R. Ahlrichs, Phys. Chem. Chem. Phys. **7**(18), 3297 (2005).
[70]R. E. Easton, D. J. Giesen, A. Welch, C. J. Cramer, and D. G. Truhlar, Theor. Chim. Acta **93**(5), 281 (1996).
[71]T. Johnson, S. Sharpe, and M. Covert, Rev. Sci. Instrum. **77**(9), 094103 (2006).
[72]M. Lepère, G. Blanquet, J. Walrand, and J. P. Bouanich, J. Mol. Struct. **517–518**, 493 (2000).
[73]C. Bray, D. Jacquemart, J. Buldyreva, N. Lacome, and A. Perrin, J. Quant. Spectrosc. Radiat. Transfer **113** (11), 1102 (2012).
[74]Z. Boussetta, F. Kwabia Tchana, and H. Aroui, J. Mol. Spectrosc. **308–309**, 33 (2015).
[75]Y. Attafi, A. B. Hassen, H. Aroui, F. K. Tchana, L. Manceron, D. Doizi, J. V. Auwera, and A. Perrin, J. Quant. Spectrosc. Radiat. Transfer **231**, 1 (2019).
[76]D. Dhib, F. K. Tchana, X. Landsheere, M. Dhib, and H. Aroui, J. Quant. Spectrosc. Radiat. Transfer **231**, 115 (2019).